



Published in final edited form as:

*Phys Chem Chem Phys.* 2017 October 18; 19(40): 27556–27569. doi:10.1039/c7cp05959k.

## Binding of protofibrillar A $\beta$ trimers to lipid bilayer surface enhances A $\beta$ structural stability and causes membrane thinning

Xuewei Dong<sup>a</sup>, Yunxiang Sun<sup>a</sup>, Guanghong Wei<sup>a</sup>, Ruth Nussinov<sup>b,c</sup>, and Buyong Ma<sup>b</sup>

<sup>a</sup>State Key Laboratory of Surface physics, Key Laboratory for Computational Physical Science (Ministry of Education), and Department of Physics, Collaborative Innovation Center of Advanced Microstructures (Nanjing), Fudan University, Shanghai 200433, People's Republic of China

<sup>b</sup>Basic Science Program, Leidos Biomedical Research, Inc. Cancer and Inflammation Program, National Cancer Institute, Frederick, Maryland 21702, USA

<sup>c</sup>Sackler Inst. of Molecular Medicine, Department of Human Genetics and Molecular Medicine, Sackler School of Medicine, Tel Aviv University, Tel Aviv 69978, Israel

### Abstract

Alzheimer's disease (AD), a common neurodegenerative disease, is characterized by the aggregation of amyloid- $\beta$  (A $\beta$ ) peptides. The interactions of A $\beta$  with membranes cause changes in membrane morphology and ion permeation, which are responsible for its neurotoxicity and can accelerate fibril growth. However, the A $\beta$ -lipid interactions and how these induce membrane perturbation and disruption at the atomic level and the consequences for the A $\beta$  organization are not entirely understood. Here, we perform multiple atomistic molecular dynamics (MD) simulations on three protofibrillar A $\beta_{9-40}$  trimers. Our simulations show that, regardless of the morphologies and the initial orientations of the three different protofibrillar A $\beta_{9-40}$  trimers, the N-terminal  $\beta$ -sheet of all trimers preferentially binds to the membrane surface. The POPG lipid bilayers enhance the structural stability of protofibrillar A $\beta$  trimers by stabilizing inter-peptide  $\beta$ -sheets and D23-K28 salt-bridges. The interaction causes local membrane thinning. We found that the trimer structure related to Alzheimer's disease brain tissue (2M4J) is the most stable both in water solution and at membrane surface, and displays slightly stronger membrane perturbation capability. These results provide mechanistic insights into the membrane-enhanced structural stability of protofibrillar A $\beta$  oligomers and the first step of A $\beta$ -induced membrane disruption at the atomic level.

### Introduction

Alzheimer's disease (AD), which was first identified more than a hundred years ago, is a neurodegenerative brain disease recognized as the prevailing cause of dementia as well as a major cause of death<sup>1</sup>. Between 2000 and 2013, deaths resulting from stroke, heart disease and cancer decreased 23%, 14%, and 11%, respectively, whereas those from Alzheimer's disease increased 71%<sup>2</sup>. The accumulation and aggregation of amyloid beta (A $\beta$ ) outside neurons (senile plaques) and abnormal tau inside neurons (neurofibrillary tangles) are considered as two biomarkers of Alzheimer's disease and are also believed to contribute to the damage of neural tissues in human brains<sup>3, 4</sup>. A $\beta$  is an intrinsically disordered protein (IDP) in solution. Compared to folded proteins, the free energy landscape of IDPs is rather

shallow, consisting of many metastable states generally separated by lower energy barriers, which allows conformational transitions to occur readily<sup>5</sup>. Thus IDPs usually have higher aggregation propensity than folded proteins<sup>6</sup>.

A $\beta$  peptide results from proteolysis of the amyloid precursor protein (APP) in the transmembrane region by  $\beta$ - and  $\gamma$ -secretase. Protease cleavage of APP at different positions by  $\gamma$ -secretase generates a variety of A $\beta$  peptides such as A $\beta$ <sub>1-37</sub>, A $\beta$ <sub>1-40</sub>, A $\beta$ <sub>1-42</sub> and A $\beta$ <sub>1-43</sub><sup>7</sup>. Previous solution NMR experiments reported that A $\beta$  monomer is largely unstructured in aqueous solution<sup>8, 9</sup>, while it can also adopt a partially folded structure with a  $3_{10}$  helix from residues H13 to D23 (PDB ID: 2LFM)<sup>10</sup>. A recent NMR study showed that A $\beta$ <sub>1-40</sub> adopts a partially helical structure upon binding to zwitterionic lipid bilayers prior to amyloid formation<sup>11</sup>. A $\beta$  monomers can readily undergo aggregation by a nucleation–elongation process leading to the formation of various oligomers and amyloid fibrils<sup>12</sup>. A $\beta$ <sub>1-42</sub> aggregates faster in vitro<sup>13</sup> and is identified as more cellular toxic than the other alloforms<sup>14</sup>, while A $\beta$ <sub>1-40</sub> levels in human brains are nearly 5 times higher than A $\beta$ <sub>1-42</sub> levels<sup>15</sup>. The main components of the senile plaques in the brains of AD patients are A $\beta$ <sub>1-40</sub> and A $\beta$ <sub>1-42</sub> peptides<sup>16</sup>, with a wide range of A $\beta$ <sub>1-40</sub>/A $\beta$ <sub>1-42</sub> ratios<sup>17</sup>. Both A $\beta$ <sub>1-40</sub> and A $\beta$ <sub>1-42</sub> are good model systems in the study of aggregation mechanism and neuronal toxicity of A $\beta$  peptides<sup>18</sup>. As demonstrated by different experimental techniques such as solid-state nuclear magnetic resonance (ssNMR) and electron microscopy, A $\beta$  fibrils are structurally polymorphic and exhibit significant differences in the extent and locations of stable  $\beta$ -sheets<sup>19–22</sup>. Several ssNMR-derived A $\beta$ <sub>1-40</sub>/A $\beta$ <sub>1-42</sub> fibril models were reported<sup>15, 23–28</sup>. Three of them have been extensively studied and their PDB IDs are 2BEG (residues 17–42 for synthetic A $\beta$ <sub>1-42</sub> fibrils)<sup>25</sup>, 2LMN (residues 9–40 for synthetic A $\beta$ <sub>1-40</sub> fibrils)<sup>26</sup> and 2M4J (residues 1–40 for AD-brain-derived A $\beta$ <sub>1-40</sub> fibrils)<sup>15</sup>. More importantly, A $\beta$  fibrils with variable structures display distinct levels of toxicity in neuronal cell cultures<sup>22, 29</sup>. Thus, studies of the interactions between different fibrils or fibril-like oligomers and membranes, especially the amyloid form found in Alzheimer's disease brain tissue (2M4J)<sup>15</sup> can illuminate important pathology-related occurrences.

Experimental studies reported that mature fibrils and intermediate aggregates of A $\beta$  are cytotoxic<sup>30–32</sup>. Toxicity is related to their interactions with the neuronal lipid bilayer<sup>33</sup>. Membranes can serve as a site for accumulation/nucleation, greatly accelerating the rate of fibrillization<sup>33, 34</sup>; but they can be disrupted in this process<sup>33, 34</sup>. Membrane thinning, pore formation and fragmentation are three possible A $\beta$ -induced membrane disruption mechanisms<sup>33–36</sup>. A $\beta$  interacts preferentially with anionic phospholipids<sup>37, 38</sup> and the disruption effect is more prominent in negatively charged membranes<sup>38–40</sup>. However, the molecular mechanism of amyloid neurotoxicity is still not fully understood.

To get mechanistic insights into membrane disruption by toxic amyloids in atomic detail, several computational groups have investigated the interactions of A $\beta$  oligomers with lipid bilayers by performing molecular dynamics (MD) simulations<sup>41–47</sup>. Jang et al examined the structural properties of modeled A $\beta$ <sub>9–42</sub>/A $\beta$ <sub>17–42</sub> channels in zwitterionic POPC lipid bilayers and obtained A $\beta$  channel conformations with diameters consistent with AFM measurements<sup>41, 48–50</sup>. Zhao et al studied the trimerization of helical A $\beta$ <sub>1-42</sub> peptide inside cholesterol-rich DPPC lipid bilayers and observed formation of short parallel  $\beta$ -sheet

structures<sup>43</sup>. MD simulations by Poojari et al. demonstrated that compared to transmembrane A $\beta$ <sub>1-42</sub> monomers, membrane-embedded  $\beta$ -sheet-rich tetramers increased the water flow through the POPC bilayers<sup>44</sup>. Brown et al. reported that the binding of disordered A $\beta$ <sub>1-42</sub> tetramers on POPC membranes resulted in a greater membrane perturbation than that on cholesterol-rich membranes<sup>47</sup>. Multiple 80-ns MD simulations by Yu et al showed that the interactions of protofibrillar A $\beta$ <sub>17-42</sub> pentamers with a mixed POPC and POPG membrane are stronger than those with POPC membranes<sup>45</sup>, indicative of the role of surface charge in A $\beta$ -membrane interactions. Recently, Tofoleanu et al explored the influence of chemical compositions of POPC and POPE headgroups on the interactions of A $\beta$ <sub>9-40</sub> protofilaments with membranes by performing MD simulations ranging from 25–150 ns. They found that POPC membranes exhibited weaker interactions with A $\beta$ <sub>9-40</sub> protofilaments than POPE<sup>51</sup>. However, a systematic study of the interactions of protofibrillar A $\beta$  oligomers with lipid bilayers that would evaluate and compare these is lacking.

In this study, we investigate how protofibrillar A $\beta$  oligomers and membranes interact with and mutually influence each other by performing extensive all-atom molecular dynamics (MD) simulations in the absence and presence of a lipid bilayer. The structures of A $\beta$ <sub>1-42</sub> have special folds due to the K28-A42 salt bridge<sup>28, 52</sup>. We focus on the A $\beta$ <sub>9-40</sub> sequence which may capture the common features of A $\beta$ <sub>40</sub> and A $\beta$ <sub>42</sub>. Three different A $\beta$ <sub>9-40</sub> trimers were constructed using the three extensively-studied ssNMR-derived fibril models (PDB ID: 2BEG, 2LMN and 2M4J) which have a U-shaped topology consisting of a  $\beta$ -sheet—turn— $\beta$ -sheet conformation<sup>15, 25, 26</sup>. 2M4J structure is found in the brain tissue of patients with Alzheimer's disease<sup>22</sup>. Using the ssNMR-derived fibrils to construct the A $\beta$ <sub>9-40</sub> trimers allows us to investigate the interactions between A $\beta$  protofibrils and membranes. These trimers were used to model the protofibrillar A $\beta$  oligomers. An anionic POPG bilayer was employed to model the phospholipid membrane. Our selection of trimer is motivated by two previous studies. A single-molecule study by Ding et al reported that trimers and tetramers may be the smallest A $\beta$ <sub>1-40</sub> oligomers in the anionic lipid bilayers and could be the origin of neurotoxicity<sup>53</sup>. A MD simulation work by Zhao et al. showed that protofibrillar A $\beta$  trimers might be the smallest seeding nucleus on the self-assembled monolayer surfaces<sup>54</sup>. We carried out four independent 200-ns MD simulations for each protofibrillar A $\beta$ <sub>9-40</sub> trimer. The initial minimum distance of between the backbone of A $\beta$  and the surface of the POPG lipid bilayer is ~0.8 nm. To avoid the bias of the initial orientation of A $\beta$ <sub>9-40</sub> trimer with respect to the POPG bilayer surface on the simulation results, we considered four different initial orientations for each protofibrillar trimer (see Table 1). Our simulations show that regardless of the conformations of the three different A $\beta$ <sub>9-40</sub> trimers and their initial orientations relative to the membrane surface, the N-terminal  $\beta$ -sheet region of A $\beta$  preferentially binds to the membrane surface due to strong electrostatic interactions between the positively charged N-terminus (NH<sub>3</sub><sup>+</sup>) and side chains of K16 residue and the negatively charged phosphate groups in the POPG head groups. The membrane-adsorbed A $\beta$ <sub>9-40</sub> trimers have higher  $\beta$ -sheet content and more salt-bridges than the trimers in water, demonstrating that the POPG membrane stabilizes the protofibrillar A $\beta$  trimers. On the other hand, the A $\beta$  trimers cause membrane perturbation by decreasing the local thickness of lipid bilayers.

## Materials and Methods

### Protofibrillar A $\beta_{9-40}$ trimers

The amino acid sequence of the 32-residue A $\beta_{9-40}$  peptide is NH $_3^+$ -GYEVHHQKLVFFAEDVGSNKGAIIGLMVGGVV-COO $^-$ . To simulate the experimental neutral pH condition, the side chain of Lys (Lys $^+$ ), Glu (Glu $^-$ ) and Asp (Asp $^-$ ) are charged. The N- and C-termini (NH $_3^+$ , COO $^-$ ) are also charged. The atomic coordinates of each A $\beta_{9-40}$  peptide were extracted respectively from the three ssNMR-derived A $\beta$  fibril models (PDB ID: 2BEG, 2LMN and 2M4J)<sup>15, 25, 26</sup>. Each peptide chain has a U-shaped conformation. 2BEG fibrils (residues 17–42) have  $\beta$ -strands at residues L17–S26 and I31–V40 and a turn region spanning residues N27–A30<sup>25</sup>, while 2LMN fibrils (residues 9–40) have  $\beta$ -strands at Y10–D23 and A30–G38 and a turn at residues V24–G29<sup>26</sup>. 2M4J Fibrils (residues 1–40) show a deformed U-shaped conformation, with  $\beta$ -strand-like regions at residues V12–F19 and I31–V36, a turn at F20–A30, a bend at G37–G38 and a more ordered N-terminal region<sup>15</sup>. In order to facilitate comparison of the structural properties of the three protofibrillar A $\beta$  trimers, in this study, the same amino acid sequence (i.e. A $\beta_{9-40}$ ) was considered for the three trimers. Thus, residues 9–16 (with sequence GYEVHHQK in  $\beta$ -strand conformation) were added to the originally published 2BEG structure, while residues 41 and 42 were removed. No modifications were done for the originally published 2LMN structure. Residues 1–8 were removed from the original 2M4J. Each protofibrillar A $\beta_{9-40}$  trimer was constructed by in-register parallel stacking of the  $\beta$ -strands (Fig. S1). For convenience, we use the PDB ID (2BEG, 2LMN and 2M4J) of each NMR-derived fibril model to denote the three A $\beta_{9-40}$  trimers (see Table 1). Note that the 2BEG and 2M4J systems used in this work were modified from the originally published pdb structures. In spite of modifications, the elongated 2BEG and truncated 2M4J still maintain respectively the structural feature of the original 2BEG and 2M4J fibrils: the U-shaped conformation stabilized respectively by inter- and intra-molecular D23–K28 salt-bridges.

### POPG lipid bilayer

The POPG lipid bilayer is composed of 2 $\times$ 100 lipids (i.e., 100 lipids in each leaflet). The initial coordinates and force field parameters are obtained from lipidbook<sup>55, 56</sup>. The initial size of the POPG bilayer is  $\sim$ 8 nm $\times$ 8 nm in the x-y plane. The molecular structure of a POPG lipid is given in Fig. S2. The properties of POPG membranes have been recently determined by MD simulations and small-angle neutron and X-ray scattering experiments, indicating that the molecular area is 66.0 $\pm$ 1.3  $\text{\AA}^2$  and the bilayer thickness is 36.7 $\pm$ 0.7  $\text{\AA}$ <sup>57</sup>. The POPG bilayer is fully anionic, and has been routinely used in experiments and simulations to probe the interaction of negatively charged membrane with various charged peptides. Beschiaschvili and Seelig studied the binding of cyclic somatostatin analogue peptides with neutral and negatively charged monolayer films<sup>58</sup>. They found that binding of the positively charged peptide and the negatively charged POPG surface was enhanced as compared to the binding to a neutral POPC membrane<sup>58</sup>. A study exploring membrane selectivity of the antimicrobial peptide KIGAKI using solid-state NMR spectroscopy found that strong electrostatic interaction between the cationic peptide KIGAKI and anionic POPG lipids is not the only factor determining the antimicrobial activity<sup>59</sup>. Nevertheless, the use of a fully anionic lipid bilayer allows us to observe A $\beta$ -membrane interactions within relatively

short simulation time scales as A $\beta$  prefers to interact with anionic lipids<sup>37, 38</sup>, thus saving computational cost.

### A $\beta$ -POPG system

Each A $\beta_{9-40}$  protofibrillar trimer was placed on the upper leaflet of the POPG, with a minimum distance of  $\sim 0.8/0.5$  nm between the backbone/all-atoms of A $\beta$  and the surface of the POPG lipid bilayer. To eliminate the bias of the initial orientation of A $\beta_{9-40}$  trimers relative to the POPG surface on the simulation results, we chose four different initial orientations for each trimer (see Table 1): N-terminal  $\beta_1$ -strand ( $\beta_1$  surface) or C-terminal  $\beta_2$ -strand ( $\beta_2$  surface) facing the lipid surface; one side of the strand-turn-strand conformation (face) or the other side of the strand-turn-strand conformation (back) orienting towards the bilayer surface. The four surfaces ( $\beta_1$ ,  $\beta_2$ , face and back) of the A $\beta$  trimers are shown in Fig. S1. Each initial orientation corresponds to an initial state of MD simulations. Thus, there are four different initial states for each A $\beta$ -POPG system. The four initial A $\beta$ -POPG states are labelled as  $\beta_1$ -to-lipid,  $\beta_2$ -to-lipid, face-to-lipid and back-to-lipid (Table 1).

### Simulation details

All MD simulations were performed in the isothermal-isobaric (NPT) ensemble using GROMACS-4.5.3 software package<sup>60</sup>. The Amber99SB force field<sup>61</sup> was used for the A $\beta_{9-40}$  trimers. The POPG lipids were described with the Jämbbeck force field<sup>56, 62, 63</sup>. During the preparation stage for the MD simulations, the A $\beta$ -POPG system was placed in the center of a rectangular box of  $8.2 \times 8.3 \times 13.7$  nm<sup>3</sup>, with the distance between A $\beta$  trimer and the box wall being  $\sim 3.0$  nm. Periodic boundary conditions were applied. Then the A $\beta$ -POPG system was fully solvated in simple point charge (SPC) water. Na<sup>+</sup> and Cl<sup>-</sup> ions were added to neutralize the system, which provides an additional 0.1 M salt concentration. Bond length of peptides and water molecules were constrained respectively using the LINCS<sup>64</sup> and SETTLE<sup>65</sup> algorithms, allowing an integration time step of 2 fs. The protein, POPG membrane and non-protein (water molecules and counterions) groups were separately coupled to an external heat bath with a relaxation time of 0.2 ps using a velocity rescaling coupling method<sup>66</sup>. The temperature of the system is kept close to 310 K, above the gel-liquid crystal phase transition temperature (271 K) of POPG bilayers<sup>67</sup>. The pressure was kept at 1 bar using the Parrinello-Rahman method<sup>68</sup> with a coupling constant of 1.0 ps. Electrostatic interactions were treated with the particle mesh Ewald (PME) method with a real space cutoff of 1.0 nm. The van der Waals interactions were calculated using a cutoff of 1.4 nm. Each system was energy-minimized by steepest descent for 50000 steps. After minimization, the solvent was equilibrated in a 100-ps NVT MD run with position restraints on the protein. The solvent equilibration was followed by another 100-ps NVT MD run without position restraints on the protein. Then a 100-ps NPT MD run was performed on the full system. This was followed by production MD runs for each system. Four independent 200-ns production MD simulations were conducted for each of the three different protofibrillar A $\beta$  trimers in the presence of POPG membrane (A $\beta$ -POPG system) (12 simulations in total). For comparison, we also carried out a 200-ns MD simulation for each A $\beta_{9-40}$  trimer in water without POPG membrane (A $\beta$  system). The name and initial state of A $\beta$  and A $\beta$ -POPG systems are given in Table 1. A summary of the MD setup details is given in Table 2.

## Analysis

The  $\beta$ -sheet content was calculated using the DSSP program<sup>69</sup>. A salt bridge is formed if the minimum distance between the side chain  $\text{COO}^-$  group of D23 and the  $\text{N}\zeta$  atom of the side chain  $\text{NH}_3^+$  group of K28 (i.e. the D23-K28 distance) is less than 0.4 nm. The thickness of the POPG bilayer was estimated by the local average of phosphor-to-phosphor distance<sup>70</sup>. All the snapshots are displayed using the VMD program<sup>71</sup>.

## Results and Discussion

### Adsorption dynamics of three protofibrillar A $\beta$ trimers on POPG lipid bilayers

To explore the interaction mechanism of protofibrillar A $\beta$  trimers with anionic lipid bilayers, we firstly investigate the adsorption behavior of each trimer on POPG bilayers. Figure 1 shows the time evolution of the minimum distance between each amino acid residue of the 2BEG trimer and the POPG bilayer and snapshots at five different time points starting from four different initial states. In the MD run with the initial state of  $\beta_1$ -to-lipid (Fig. 1(a)), the turn region (residues G25-K28) is adsorbed on the bilayer first, followed by the N-terminal residues G9-K16, resulting in membrane binding of the  $\beta_1$  and turn regions. This observation is not surprising as the simulation started from the  $\beta_1$ -to-lipid state. In the MD runs initiating from  $\beta_2$ -to-lipid (Fig. 1(b)), face-to-lipid (Fig. 1(c)) and back-to-lipid (Fig. 1(d)), the N-terminal residues G9-H14 are adsorbed on the bilayer surface first, then residues Q15-K28 in the  $\beta_1$  region sequentially bind. This leads to the binding of the full  $\beta_1$  region and the turn region to the membrane surface. Of particular interest is the adsorption process observed in Fig. 1(b) that although C-terminal residues initially face towards the membrane surface, the A $\beta$  trimer still rotates itself and the N-terminal residues bind to the lipid bilayer. Overall, irrespective of the initial orientations, it is the  $\beta_1$  region (containing positively-charged N-terminus  $\text{NH}_3^+$  and residues K16) or the turn region (containing positively-charged residues K28) that initiate the adsorption, which results in the binding of  $\beta_1$ +turn region of 2BEG trimer to the lipid bilayers (see the snapshots at  $t=200$  ns in Fig. 1).

The adsorption dynamics of the 2LMN trimer to the POPG bilayer is shown in Fig. 2. In the two MD runs starting from  $\beta_1$ -to-lipid (Fig. 2(a)) and face-to-lipid (Fig. 2(c)), the N-terminal residues G9-H14 bind to the bilayer surface first, followed by residues Q15-K28, leading to membrane binding of the  $\beta_1$ +turn region of the 2LMN trimer (snapshots in Fig. 2(a, c)). When starting from  $\beta_2$ -to-lipid (Fig. 2(b)) and back-to-lipid (Fig. 2(d)), the adsorption to the POPG bilayer surface is initiated from the turn region (residues G25-K28). Only the turn region binds to the POPG surface within the 200 ns of these two MD runs, indicating that a long time is needed for the adsorption of  $\beta_1$  region on POPG bilayers. The detailed process can be seen from snapshots at five time points in Fig. 2.

Fig. 3 shows the adsorption behavior of the 2M4J trimer onto the POPG bilayer. In the two runs starting from  $\beta_1$ -to-lipid (Fig. 3(a)) and back-to-lipid (Fig. 3(d)), the adsorption is initiated from the N-terminal residues G9-H14. At the beginning of the  $\beta_2$ -to-lipid simulation (Fig. 3(b)), residues in  $\beta_2$  and turn regions are quite close to the membrane surface, and at  $t=18$  ns N27 residues bind to the bilayer. Shortly afterwards, the trimer rotates and the turn region dissociates from the bilayer, and then N-terminal residues G9-

Y10 anchor into the bilayer. This is followed by sequential membrane binding of other residues in  $\beta_1$  region and of the turn region, leading to the  $\beta_1$ +turn region binding. This binding event indicates that the  $\beta_1$  region has a preference to bind to the POPG bilayer although initially  $\beta_2$  and turn regions have atomic contacts with the bilayer. For the face-to-lipid (Fig. 3(c)), it appears that the whole A $\beta$  trimer comes close to the membrane surface at first. After that, N-terminal residues keep contacts with the bilayer, while C-terminal residues in the  $\beta_2$  region gradually dissociate. The detailed process can be seen from the snapshots at five time points in Fig. 3.

By comparing all the simulation results, we find that the three distinct trimers display similar adsorption behaviors, regardless of their structural morphologies and initial orientations. Namely, N-terminal residues G9-K16 in  $\beta_1$  region preferentially bind to the membrane surface, followed by other residues in the  $\beta_1$  and turn regions, leading to the binding of  $\beta_1$ +turn region of A $\beta$  trimer onto the lipid bilayers. This finding indicates that our simulation results do not depend on the initial states of A $\beta$ -POPG systems. In term of absorption rate of the N-terminal  $\beta_1$  region, the three trimer forms are in the order of 2M4J > 2BEG > 2LMN.

To identify the key residues that bind to the POPG bilayer, we calculated the binding probability of each residue for the three trimers (Fig. 4). Our calculation shows that N-terminal residues G9-K16 (containing the positively charged N-terminal  $\text{NH}_3^+$  and residues K16) in the  $\beta_1$  region exhibit the highest membrane binding probability and turn region G25-G29 (containing positively charged residues) display the second highest binding probability. These results indicate that electrostatic interaction is an important driving force to facilitate the adsorption on the anionic membrane. This finding is consistent with previous studies showing that electrostatic interactions with negatively charged lipids enhance peptide adsorption onto lipid monolayers/bilayers<sup>45, 72</sup>. The relative higher membrane binding probabilities of the residues in the N-terminal  $\beta_1$  region also suggest strong interactions between N-terminal residues of A $\beta$  trimers and POPG bilayers.

### The influence of POPG bilayers on the structural stabilities of the A $\beta$ trimers

We conducted a 200-ns MD simulation for each trimer in water without the lipid bilayers. Fig. 5(a) and (b) show respectively the time evolution of the root-mean-square deviation (RMSD) of each trimer with respect to its initial conformation and the number of backbone hydrogen bonds. It can be seen from Fig. 5 that the RMSDs of the three trimers all reach a plateau after  $t=110$  ns and their values are 0.8 nm for 2BEG, 1.1 nm for 2LMN and 0.5 nm for 2M4J. The RMSD values reflect different structural stabilities in water: the 2M4J trimer is the most stable, 2BEG is the less stable and 2LMN is the least stable. This finding is supported by the time evolution of the number of backbone hydrogen bonds (H-bonds) in Fig. 5(b). Namely, 2M4J has the largest number of H-bonds (note that it still increases with simulation time), 2BEG has the less and 2LMN has the least. The different structural stabilities in water can be clearly seen from the snapshots of A $\beta$  trimer generated at  $t=0$ , 100 and 200 ns (Fig. 5(c, d, e)). The 2M4J trimer keeps its protofibrillar structure during the full process of the 200-ns MD simulation. The increase of its RMSD value with simulation time

(blue curve in Fig. 5(a)) mainly results from the twisting of the three strands with respect to each other (see the snapshots at  $t=100$  and  $200$  ns in Fig. 5(e)).

The structural stability of each protofibrillar  $A\beta_{9-40}$  trimer in the presence of POPG lipid bilayers are investigated by monitoring the time evolution of the  $C_{\alpha}$ -RMSD and the number of backbone H-bonds of  $A\beta$  trimer in MD runs starting from four different initial states (Fig. 6). For comparison, the time evolution of these two parameters for each  $A\beta$  trimer in water without POPG bilayers are also given (black curve). It can be seen from Fig. 6 that the  $C_{\alpha}$ -RMSDs and backbone H-bond number of the three trimers reach a plateau after  $t=50$  ns for 2BEG and after  $100$  ns for both 2LMN and 2M4J, indicating our simulations are reasonably converged. Figure 6(a, b, c) shows that 2BEG, 2LMN and 2M4J trimers have different RMSD values, implying their different structural stabilities on the POPG bilayer surface. 2M4J trimer is the most stable (with the smallest RMSD), 2BEG trimer is the less stable (larger RMSD) and 2LMN trimer is the least stable (with the largest RMSD value). The 2BEG and 2LMN trimers on the bilayer surface have smaller RMSD values and more backbone H-bonds than the trimers in water (Fig. 6(a, b, d, e)). The results reveal that membrane-bound protofibrillar 2BEG and 2LMN trimers are more stable than  $A\beta$  trimers in aqueous solution, highlighting the role of POPG bilayer in stabilizing the structures of  $A\beta$  trimers. In the MD run starting from  $\beta_2$ -to-lipid (green curve in Fig. 6(a)), the RMSD value of the membrane-bound 2BEG trimer is almost the same as that of the isolated trimer in water, due to the slow adsorption of the trimer on the bilayer surface (see Fig. 1(b)). We also found that the RMSD values and the number of H-bonds of the membrane-bound 2M4J trimer resembles those of the trimer in water (Fig. 6(c, f)), implying that the 2M4J trimer on POPG has similar structural stability as in water. The small RMSD values ( $\sim 0.5$  nm) of 2M4J trimer in Fig. 6(c), together with the snapshots in Fig. 3 and Fig. 5(e), demonstrate that the 2M4J trimer is structurally stable both on the POPG membrane surface and in water. Thus, the POPG bilayer has minor influence on the structure of the 2M4J trimer. Overall, POPG bilayers can stabilize the protofibrillar  $A\beta$  trimers although the stabilization effect of the bilayer on 2M4J is not as obvious as that on 2BEG and 2LMN.

To identify the residues that contribute most to the structural stability of each trimer in the presence of POPG bilayers, we calculate the  $\beta$ -sheet propensity of each amino acid residue (red curves in Fig. 7). For each trimer, residue-based  $\beta$ -sheet propensity is obtained by averaging the  $\beta$ -sheet probability of each residue over the data in the four MD trajectories. For comparison, the  $\beta$ -sheet propensity for each trimer in water without POPG bilayers are also calculated (black curves in Fig. 7). We see from Fig. 7 that the  $\beta$ -sheet propensities of most residues in the  $\beta_1$  region of  $A\beta$  in the  $A\beta$ -POPG system are higher than those in water, while the  $\beta$ -sheet propensities of most of the residues in the  $\beta_2$  region are only slightly affected. This can also be seen from the time evolution of the secondary structure of each residue in the three MD runs for  $A\beta$  and in the 12 MD runs for  $A\beta$ -POPG system (Fig. S3). This result, together with the residue-based membrane binding probability in Fig. 4, indicates that membrane binding stabilizes the  $\beta$ -sheet structure of the N-terminal residues, which is favorable for the structural stability of  $A\beta$  trimers, especially for 2BEG and 2LMN trimers.



Previous experimental and computational studies suggested that D23-K28 salt-bridges enhance the fibrillization rate<sup>73, 74</sup> and stabilize A $\beta$  fibril structures<sup>15, 24–26</sup>. To examine whether POPG bilayers affect the D23-K28 salt-bridges, we calculate the PDF (probability density function) of the D23-K28 distance (including both intra- and inter-peptide D23-K28 distances) in isolated (black curves in Fig. 8) and in membrane-bound A $\beta$  trimers (red curves in Fig. 8). The D23-K28 distance in A $\beta$ -POPG system is the average of the four different MD runs. The PDF of the D23-K28 distance in each MD run for A $\beta$  and A $\beta$ -POPG systems are presented in Fig. S4. Two peaks (Fig. 8(a, b), black curves) are observed for the isolated 2BEG and 2LMN trimers: a small sharp peak centered at 0.28 nm and a broad peak around 0.6 nm. The probability density distribution of the two peaks implies that the D23-K28 salt-bridges in the isolated 2BEG and 2LMN trimers are almost lost. In the A $\beta$ -POPG system, the peak at 0.28 nm becomes much larger (red curves in Fig. 8(a, b)), implying that most of the D23-K28 salt bridges are preserved in the membrane-bound trimers and the interaction of A $\beta$  trimers with POPG bilayers protects the salt bridges. The peak at 0.28 nm in the membrane-bound 2M4J trimer also becomes larger than that in the isolated trimer (Fig. 8(c)), indicative of the stabilizing role of POPG bilayers on the D23-K28 salt-bridges in the 2M4J trimer. These results demonstrate that POPG bilayers stabilize the D23-K28 salt bridges that were reported to play a crucial role in A $\beta$  fibrillization<sup>73, 74</sup>.

Altogether, our simulations demonstrate that protofibrillar A $\beta$ <sub>9–40</sub> trimers become much more stable upon binding to the POPG bilayer. It is expected that the membrane-stabilized trimers would enhance the fibril formation. Consistent with our prediction, recent studies reported that A $\beta$  fibrillation can be accelerated in the presence of anionic lipid membranes<sup>33, 34</sup>.

### The influence of protofibrillar A $\beta$ trimers binding on POPG bilayers

Membrane integrity is essential for cellular activities. To investigate the perturbation of the POPG bilayers incurred by binding of the trimers, we calculated the bilayer thickness distribution in the x-y plane for each A $\beta$ -POPG system in the MD runs starting from  $\beta_1$ -to-lipid,  $\beta_2$ -to-lipid, face-to-lipid and back-to-lipid. The bilayer thickness distribution map is presented in Fig. 9. For comparison, the distribution map of a pure POPG bilayer is also given (Fig. 9(a)). The color bar from red to white represents the bilayer thickness decreasing from 3.7 to 3.2 nm. We see from Fig. 9(a) that pure POPG bilayer is almost uniform with a thickness of 3.7 nm. In contrast, the A $\beta$ -POPG system exhibits obvious local membrane thinning (the white region in Fig. 9(b–m)) except for the bilayer in Fig. 9(g) and (i). In the two MD runs corresponding to Fig. 9(g) and (i), only the turn region is adsorbed on the POPG bilayer surface (see the snapshots at  $t=200$  ns in Fig. 2(b) and (d)), while both the N-terminal  $\beta_1$  region and the turn region bind to the bilayer surface in all other MD runs. This observation, together with the different bilayer thickness distribution seen in Fig. 9 reveals that the membrane binding of protofibrillar A $\beta$  trimers results in bilayer thinning and that it is the  $\beta_1$ -POPG interaction that contributes mostly to the membrane thinning. This finding is consistent with a recent study showing that the susceptibility of neuronal cells to different types of oligomeric assemblies is directly related to the extent of binding of such oligomers to the cellular membrane<sup>75</sup>.

We then calculated the lipid tail order parameter  $S_{CD}$  for lipids in the upper leaflet using the formula  $S_{CD}=0.5 \langle 3\cos^2 \theta-1 \rangle$ , where  $\theta$  is the angle between the bilayer normal and the C-H bond vector (in the simulations) or the C-D bond vector (in experiments)<sup>76</sup>. The angular brackets denote a time and lipid ensemble average<sup>76, 77</sup>. Figure 10(a, b) gives the absolute  $S_{CD}$  values of acyl chain 1 and 2 (i.e. *sn*-1 and *sn*-2) of POPG lipids in each A $\beta$ -POPG system. The *sn*-1 and *sn*-2 chains and the carbon atoms in the two chains are labelled in Fig. S2. For comparison, the  $S_{CD}$  values of the two chains from a 200 ns MD run of a pure POPG lipid bilayer are also given in Fig. 10(a, b). We see from Fig. 10(a) that the  $S_{CD}$  values of *sn*-1 chains in all A $\beta$ -POPG systems are close to each other, but slightly smaller than those in a pure POPG bilayer. We noted that 2M4J (green line) leads to the lowest  $S_{CD}$  values, indicating larger membrane perturbation. The differences among the  $S_{CD}$  values of *sn*-2 chains in all systems are negligible. Consistent with the change of  $S_{CD}$  values of *sn*-1 chains, the lipid area in each A $\beta$ -POPG system becomes slightly larger than that in the pure POPG system, with 2M4J being the most obvious again (Fig. 10(c)). These results indicate that while membrane binding of protofibrillar A $\beta$  trimers does not significantly impact the ordering of the POPG bilayer within our simulation time scale, structural polymorphism may still have different membrane perturbation effects. To examine whether the A $\beta$ -induced membrane perturbation can cause water penetration into the POPG bilayer, we calculated the water density distribution along the membrane normal (i.e. the z-axis direction) for each A $\beta$ -POPG system (Fig. S5). For comparison, the water density distribution along the membrane normal in a pure POPG bilayer is also given. The membrane center is at  $z=0$  nm and the thickness of the hydrophobic tail region is  $\sim 2.8$  nm (from  $z = -1.4$  to  $1.4$  nm). The trimer binds on the upper surface ( $z = \sim 1.7$  nm) of the POPG bilayer. As in the pure POPG system, the water density in the central hydrophobic tail region (from  $z = -1.0$  to  $1.0$  nm) of POPG bilayer in the A $\beta$ -POPG system is almost zero, indicating that membrane perturbation is not able to cause water penetration into the POPG bilayer within our simulation time scale. This finding suggests that binding alone is not sufficient for membrane permeabilization, consistent with a previous Förster resonance energy transfer (FRET) study showing that A $\beta$  membrane binding and permeabilization are distinct processes influenced separately by membrane charge and fluidity<sup>38</sup>.

Membrane thinning, pore formation and membrane fragmentation have been considered as three possible mechanisms of A $\beta$ -induced membrane disruption<sup>33-36</sup>. Our simulations demonstrate that binding of protofibrillar A $\beta$  trimers results in membrane thinning. Reduced thickness regulates the aggregation and cytotoxicity of A $\beta$ <sup>78</sup>. As membrane binding is the initial step of A $\beta$ -membrane interaction, we propose that membrane thinning might be the first step of A $\beta$ -induced membrane disruption and this will result in pore formation or membrane fragmentation.

We note that there are some limitations in this work. For example, we used a fully anionic POPG lipid bilayer to model the membrane in order to observe A $\beta$ -membrane interactions within relatively short time scale of simulations due to the large size of the simulated system. We used A $\beta_{9-40}$  (an elongated 2BEG and a truncated 2M4J) trimers to model the full-length A $\beta$  trimers in order to facilitate comparison of the structural properties of the three protofibrillar A $\beta$  trimers in the absence and presence of phospholipid bilayers and to save computational cost. Finally, due to the short time scale of MD simulations, only the

turn region of the 2LMN trimer binds to the POPG surface within the 200 ns of MD runs, while most of part of the trimers are exposed to water (Fig. 2(b, d)). Thus, it is desirable to study A $\beta$ -protofibril-membrane interactions by employing a realistic model membrane (such as a mixed POPC and POPG bilayer) and full-length A $\beta$  protofibrils and by performing long time scale MD simulations. This remains to be determined in a future study.

## Conclusions

We have systematically investigated the interactions between anionic lipid bilayers and protofibrillar A $\beta$ <sub>9-40</sub> trimers constructed using the three NMR-derived fibril structures, 2BEG, 2LMN and 2M4J, by carrying out all-atom molecular dynamics simulations. We particularly focused on the adsorption dynamics of the trimers, the effect of POPG lipid bilayers on the stability of trimers, and the perturbation of the membrane induced by the interactions of A $\beta$  with the lipid bilayers. Simulations starting from four states of each A $\beta$ -POPG system reveal that irrespective of their structural details and initial orientations, the three distinct protofibrillar A $\beta$  trimers display similar adsorption dynamics. N-terminal residues G9-K16 in  $\beta_1$  region preferentially bind to the membrane surface, followed by other residues in the  $\beta_1$  and turn regions, leading to the binding of  $\beta_1$ +turn region of A $\beta$  trimer to the lipid bilayers. This adsorption behavior is mostly dominated by the electrostatic interaction between positively charged residues and negatively charged POPG lipid bilayers. Lipid bilayers enhance the structural stability of A $\beta$  trimers by stabilizing the  $\beta$ -sheet content and the D23-K28 salt-bridges. On the other hand, the POPG lipid bilayer is also influenced by the binding of protofibril A $\beta$  trimers. A $\beta$  binding decreases the local thickness, leading to membrane thinning which is related to aggregation and toxicity of A $\beta$  peptides<sup>78</sup>. In particular, A $\beta$  structure found in Alzheimer's disease brain tissue (2M4J) is the most stable both in water solution and on membrane surface, and exhibits slightly stronger membrane perturbation ability. This investigation shows that peptide-membrane interaction can induce membrane thinning which is responsible for A $\beta$  toxicity and suggests that the membrane may promote A $\beta$  fibril growth by enhancing the structural stability of A $\beta$  oligomers, ultimately providing insights into A $\beta$ -lipid interaction and the mechanism of lipid perturbation by A $\beta$  protofibrils at atomic level.

## Supplementary Material

Refer to Web version on PubMed Central for supplementary material.

## Acknowledgments

This work has been supported by the MOST of China (Grant No. 2016YFA0501702) and the NSF of China (Grant No. 11674065). It has also been funded in whole or in part with Federal funds from the Frederick National Laboratory for Cancer Research, National Institutes of Health, under contract HHSN261200800001E. This research was supported [in part] by the Intramural Research Program of NIH, Frederick National Lab, Center for Cancer Research. The content of this publication does not necessarily reflect the views or policies of the Department of Health and Human Services, nor does mention of trade names, commercial products or organizations imply endorsement by the US Government.

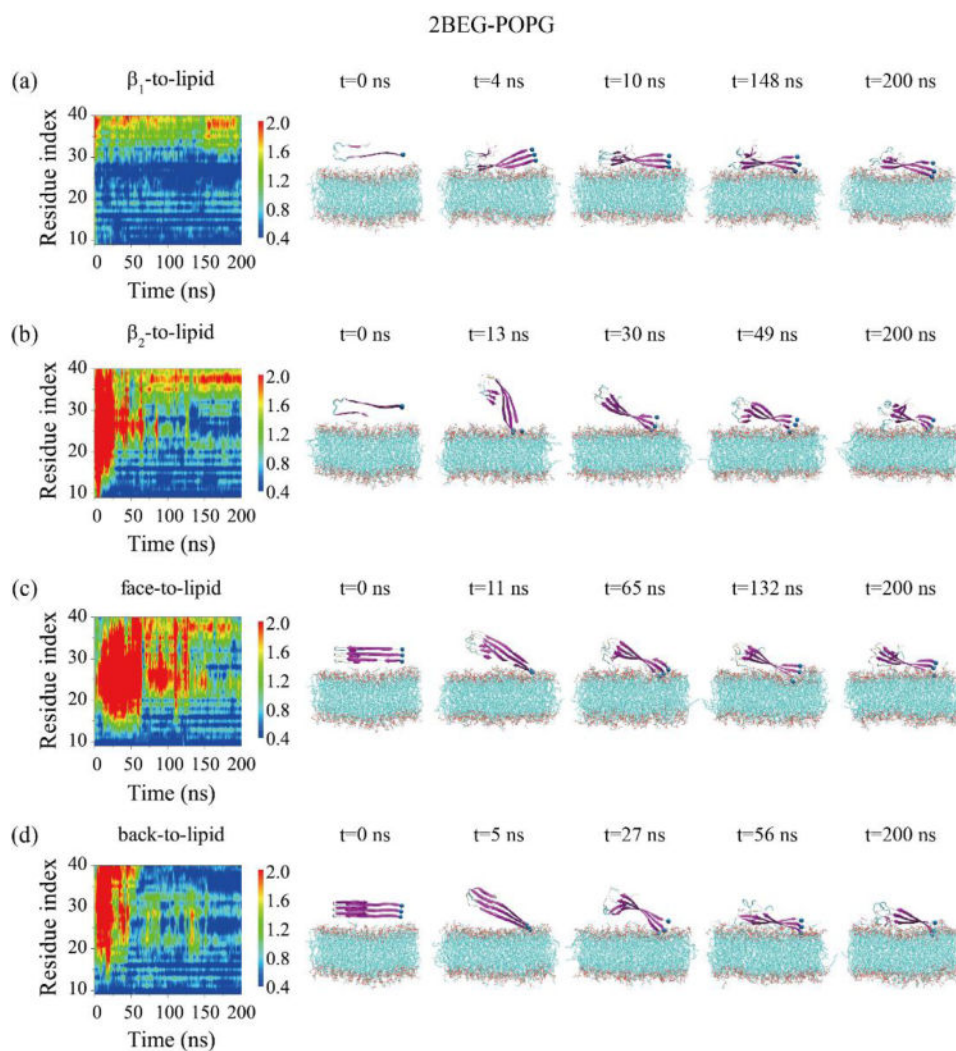
All simulations reported in this work had been performed using the high-performance computational facilities at the National High Performance Computing Center of Fudan University.

## References

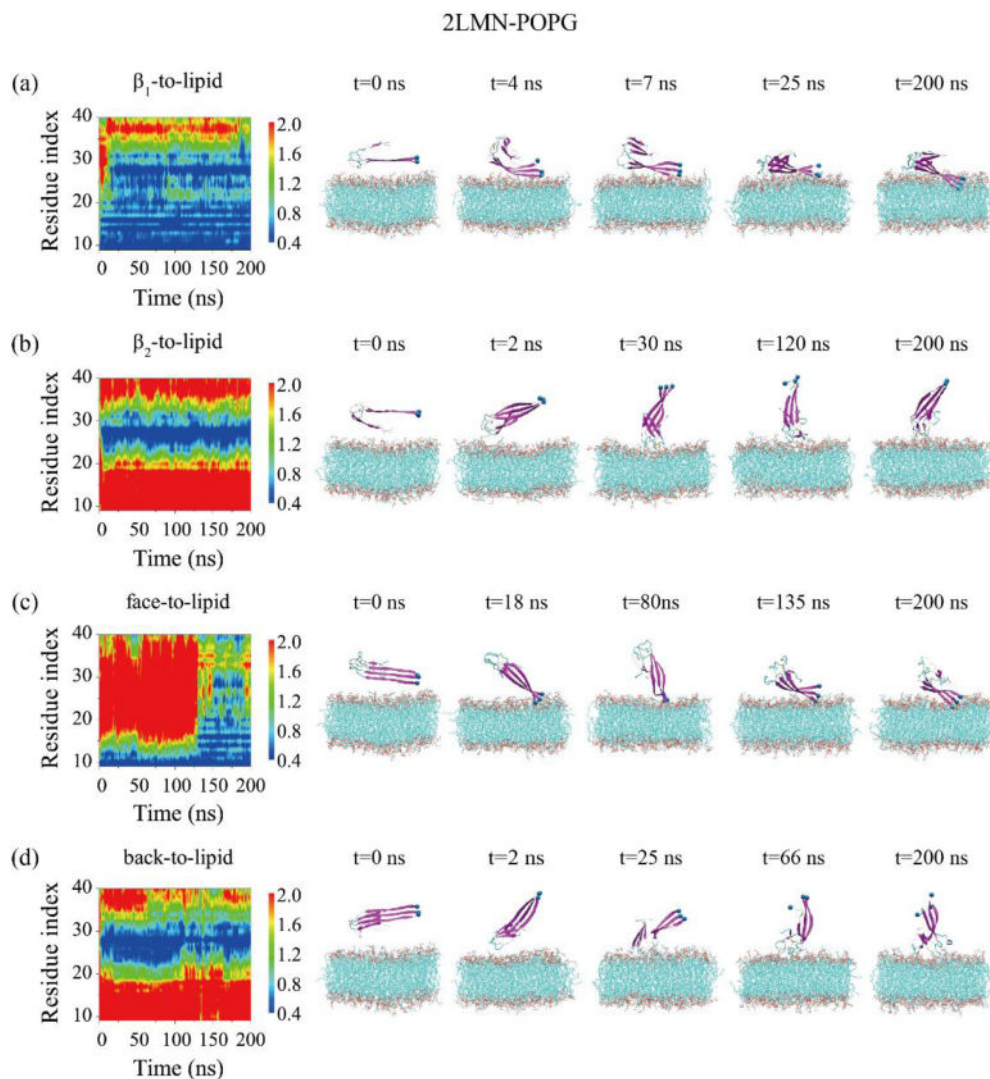
1. Wilson RS, Segawa E, Boyle PA, Anagnos SE, Hizez LP, Bennett DA. *Psychology and aging*. 2012; 27:1008–1017. [PubMed: 22946521]
2. *Alzheimer's & dementia : the journal of the Alzheimer's Association*. 2016; 12:459–509.
3. LaFerla FM, Green KN, Oddo S. *Nature reviews Neuroscience*. 2007; 8:499–509. [PubMed: 17551515]
4. Ballatore C, Lee VM, Trojanowski JQ. *Nature reviews Neuroscience*. 2007; 8:663–672. [PubMed: 17684513]
5. Wei G, Xi W, Nussinov R, Ma B. *Chem Rev*. 2016; 116:6516–6551. [PubMed: 26807783]
6. Uversky VN, Dave V, Iakoucheva LM, Malaney P, Metallo SJ, Pathak RR, Joerger AC. *Chemical reviews*. 2014; 114:6844–6879. [PubMed: 24830552]
7. Selkoe DJ. *Nature*. 1999; 399:A23–31. [PubMed: 10392577]
8. Hou L, Shao H, Zhang Y, Li H, Menon NK, Neuhaus EB, Brewer JM, Byeon IJ, Ray DG, Vitek MP, Iwashita T, Makula RA, Przybyla AB, Zagorski MG. *Journal of the American Chemical Society*. 2004; 126:1992–2005. [PubMed: 14971932]
9. Lazo ND, Grant MA, Condron MC, Rigby AC, Teplow DB. *Protein science : a publication of the Protein Society*. 2005; 14:1581–1596. [PubMed: 15930005]
10. Vivekanandan S, Brender JR, Lee SY, Ramamoorthy A. *Biochemical and biophysical research communications*. 2011; 411:312–316. [PubMed: 21726530]
11. Korshavn KJ, Bhunia A, Lim MH, Ramamoorthy A. *Chemical communications (Cambridge, England)*. 2016; 52:882–885.
12. Grant MA, Lazo ND, Lomakin A, Condron MM, Arai H, Yamin G, Rigby AC, Teplow DB. *Proceedings of the National Academy of Sciences of the United States of America*. 2007; 104:16522–16527. [PubMed: 17940047]
13. Bitan G, Kirkitadze MD, Lomakin A, Vollers SS, Benedek GB, Teplow DB. *Proc Natl Acad Sci U S A*. 2003; 100:330–335. [PubMed: 12506200]
14. Dahlgren KN, Manelli AM, Stine WB Jr, Baker LK, Krafft GA, LaDu MJ. *The Journal of biological chemistry*. 2002; 277:32046–32053. [PubMed: 12058030]
15. Lu JX, Qiang W, Yau WM, Schwieters CD, Meredith SC, Tycko R. *Cell*. 2013; 154:1257–1268. [PubMed: 24034249]
16. Pitschke M, Prior R, Haupt M, Riesner D. *Nature medicine*. 1998; 4:832–834.
17. Gravina SA, Ho L, Eckman CB, Long KE, Otvos L Jr, Younkin LH, Suzuki N, Younkin SG. *The Journal of biological chemistry*. 1995; 270:7013–7016. [PubMed: 7706234]
18. Nastica-Labouze J, Nguyen PH, Sterpone F, Berthoumieu O, Buchete NV, Cote S, De Simone A, Doig AJ, Faller P, Garcia A, Laio A, Li MS, Melchionna S, Mousseau N, Mu Y, Paravastu A, Pasquali S, Rosenman DJ, Strodel B, Tarus B, Viles JH, Zhang T, Wang C, Derreumaux P. *Chemical reviews*. 2015; 115:3518–3563. [PubMed: 25789869]
19. Bertini I, Gonnelli L, Luchinat C, Mao J, Nesi A. *Journal of the American Chemical Society*. 2011; 133:16013–16022. [PubMed: 21882806]
20. Meinhardt J, Sachse C, Hortschansky P, Grigorieff N, Fandrich M. *Journal of molecular biology*. 2009; 386:869–877. [PubMed: 19038266]
21. Kodali R, Williams AD, Chemuru S, Wetzel R. *J Mol Biol*. 2010; 401:503–517. [PubMed: 20600131]
22. Tycko R. *Neuron*. 2015; 86:632–645. [PubMed: 25950632]
23. Ma B, Nussinov R. *Proceedings of the National Academy of Sciences of the United States of America*. 2002; 99:14126–14131. [PubMed: 12391326]
24. Petkova AT, Ishii Y, Balbach JJ, Antzutkin ON, Leapman RD, Delaglio F, Tycko R. *Proc Natl Acad Sci U S A*. 2002; 99:16742–16747. [PubMed: 12481027]
25. Luhrs T, Ritter C, Adrian M, Riek-Loher D, Bohrmann B, Dobeli H, Schubert D, Riek R. *Proc Natl Acad Sci U S A*. 2005; 102:17342–17347. [PubMed: 16293696]
26. Petkova AT, Yau WM, Tycko R. *Biochemistry*. 2006; 45:498–512. [PubMed: 16401079]

27. Paravastu AK, Leapman RD, Yau WM, Tycko R. *Proc Natl Acad Sci U S A*. 2008; 105:18349–18354. [PubMed: 19015532]
28. Xiao Y, Ma B, McElheny D, Parthasarathy S, Long F, Hoshi M, Nussinov R, Ishii Y. *Nat Struct Mol Biol*. 2015; 22:499–505. [PubMed: 25938662]
29. Petkova AT, Leapman RD, Guo Z, Yau WM, Mattson MP, Tycko R. *Science (New York, NY)*. 2005; 307:262–265.
30. Li S, Hong S, Shepardson NE, Walsh DM, Shankar GM, Selkoe D. *Neuron*. 2009; 62:788–801. [PubMed: 19555648]
31. Benilova I, Karran E, De Strooper B. *Nature neuroscience*. 2012; 15:349–357. [PubMed: 22286176]
32. Lesne SE, Sherman MA, Grant M, Kuskowski M, Schneider JA, Bennett DA, Ashe KH. *Brain : a journal of neurology*. 2013; 136:1383–1398. [PubMed: 23576130]
33. Kotler SA, Walsh P, Brender JR, Ramamoorthy A. *Chemical Society reviews*. 2014; 43:6692–6700. [PubMed: 24464312]
34. Butterfield SM, Lashuel HA. *Angewandte Chemie (International ed in English)*. 2010; 49:5628–5654. [PubMed: 20623810]
35. Sciacca MF, Kotler SA, Brender JR, Chen J, Lee DK, Ramamoorthy A. *Biophysical journal*. 2012; 103:702–710. [PubMed: 22947931]
36. Jang H, Arce FT, Ramachandran S, Kagan BL, Lal R, Nussinov R. *Chemical Society reviews*. 2014; 43:6750–6764. [PubMed: 24566672]
37. Alarcon JM, Brito JA, Hermosilla T, Atwater I, Mears D, Rojas E. *Peptides*. 2006; 27:95–104. [PubMed: 16139931]
38. Wong PT, Schauerte JA, Wissner KC, Ding H, Lee EL, Steel DG, Gafni A. *Journal of molecular biology*. 2009; 386:81–96. [PubMed: 19111557]
39. Williams TL, Serpell LC. *The FEBS journal*. 2011; 278:3905–3917. [PubMed: 21722314]
40. Sabate R, Espargaro A, Barbosa-Barros L, Ventura S, Estelrich J. *Biochimie*. 2012; 94:1730–1738. [PubMed: 22542639]
41. Jang H, Arce FT, Capone R, Ramachandran S, Lal R, Nussinov R. *Biophysical journal*. 2009; 97:3029–3037. [PubMed: 19948133]
42. Chang Z, Luo Y, Zhang Y, Wei G. *The journal of physical chemistry B*. 2011; 115:1165–1174. [PubMed: 21192698]
43. Zhao LN, Chiu SW, Benoit J, Chew LY, Mu Y. *The journal of physical chemistry B*. 2011; 115:12247–12256. [PubMed: 21910473]
44. Poojari C, Kukol A, Strodel B. *Biochimica et biophysica acta*. 2013; 1828:327–339. [PubMed: 22975281]
45. Yu X, Wang Q, Pan Q, Zhou F, Zheng J. *Physical chemistry chemical physics : PCCP*. 2013; 15:8878–8889. [PubMed: 23493873]
46. Tofoleanu F, Buchete NV. *Journal of molecular biology*. 2012; 421:572–586. [PubMed: 22281438]
47. Brown AM, Bevan DR. *Biophysical journal*. 2016; 111:937–949. [PubMed: 27602722]
48. Jang H, Teran Arce F, Ramachandran S, Capone R, Lal R, Nussinov R. *The journal of physical chemistry B*. 2010; 114:9445–9451. [PubMed: 20608696]
49. Jang H, Arce FT, Ramachandran S, Capone R, Lal R, Nussinov R. *Journal of molecular biology*. 2010; 404:917–934. [PubMed: 20970427]
50. Jang H, Zheng J, Lal R, Nussinov R. *Trends Biochem Sci*. 2008; 33:91–100. [PubMed: 18182298]
51. Tofoleanu F, Brooks BR, Buchete NV. *ACS chemical neuroscience*. 2015; 6:446–455. [PubMed: 25581460]
52. Colvin MT, Silvers R, Ni QZ, Can TV, Sergeyev I, Rosay M, Donovan KJ, Michael B, Wall J, Linse S, Griffin RG. *Journal of the American Chemical Society*. 2016; 138:9663–9674. [PubMed: 27355699]
53. Ding H, Schauerte JA, Steel DG, Gafni A. *Biophysical journal*. 2012; 103:1500–1509. [PubMed: 23062342]

54. Zhao J, Wang Q, Liang G, Zheng J. *Langmuir : the ACS journal of surfaces and colloids*. 2011; 27:14876–14887. [PubMed: 22077332]
55. Domanski J, Stansfeld PJ, Sansom MS, Beckstein O. *The Journal of membrane biology*. 2010; 236:255–258. [PubMed: 20700585]
56. Jambeck JP, Lyubartsev AP. *Journal of chemical theory and computation*. 2013; 9:774–784. [PubMed: 26589070]
57. Kucerka N, Holland BW, Gray CG, Tomberli B, Katsaras J. *J Phys Chem B*. 2012; 116:232–239. [PubMed: 22107350]
58. Beschiaschvili G, Seelig J. *Biochemistry*. 1990; 29:10995–11000. [PubMed: 2271694]
59. Lu JX, Blazyk J, Lorigan GA. *Biochim Biophys Acta*. 2006; 1758:1303–1313. [PubMed: 16537078]
60. Hess B, Kutzner C, van der Spoel D, Lindahl E. *Journal of chemical theory and computation*. 2008; 4:435–447. [PubMed: 26620784]
61. Hornak V, Abel R, Okur A, Strockbine B, Roitberg A, Simmerling C. *Proteins*. 2006; 65:712–725. [PubMed: 16981200]
62. Jambeck JP, Lyubartsev AP. *The journal of physical chemistry B*. 2012; 116:3164–3179. [PubMed: 22352995]
63. Jambeck JP, Lyubartsev AP. *Journal of chemical theory and computation*. 2012; 8:2938–2948. [PubMed: 26592132]
64. Hess B, Bekker H, Berendsen HJ, Fraaije JG. *Journal of computational chemistry*. 1997; 18:1463–1472.
65. Miyamoto S, Kollman PA. *Journal of computational chemistry*. 1992; 13:952–962.
66. Bussi G, Donadio D, Parrinello M. *The Journal of chemical physics*. 2007; 126:014101. [PubMed: 17212484]
67. Wiedmann T, Salmon A, Wong V. *Biochimica et biophysica acta*. 1993; 1167:114–120. [PubMed: 8466937]
68. Parrinello M, Rahman A. *Journal of Applied Physics*. 1981; 52:7182–7190.
69. Kabsch W, Sander C. *Biopolymers*. 1983; 22:2577–2637. [PubMed: 6667333]
70. Elmore DE. *FEBS letters*. 2006; 580:144–148. [PubMed: 16359668]
71. Humphrey W, Dalke A, Schulten K. *Journal of molecular graphics*. 1996; 14:33–38. 27–38. [PubMed: 8744570]
72. Maltseva E, Kerth A, Blume A, Mohwald H, Brezesinski G. *Chembiochem : a European journal of chemical biology*. 2005; 6:1817–1824. [PubMed: 16175542]
73. Sciarretta KL, Gordon DJ, Petkova AT, Tycko R, Meredith SC. *Biochemistry*. 2005; 44:6003–6014. [PubMed: 15835889]
74. Reddy G, Straub JE, Thirumalai D. *The journal of physical chemistry B*. 2009; 113:1162–1172. [PubMed: 19125574]
75. Evangelisti E, Cascella R, Becatti M, Marrazza G, Dobson CM, Chiti F, Stefani M, Cecchi C. *Scientific reports*. 2016; 6:32721. [PubMed: 27619987]
76. Vermeer LS, de Groot BL, Reat V, Milon A, Czaplicki J. *European biophysics journal : EBJ*. 2007; 36:919–931. [PubMed: 17598103]
77. Zhang Y, Luo Y, Deng Y, Mu Y, Wei G. *PloS one*. 2012; 7:e38191. [PubMed: 22693597]
78. Korshavn KJ, Satriano C, Lin Y, Zhang R, Dulchavsky M, Bhunia A, Ivanova MI, Lee YH, La Rosa C, Lim MH, Ramamoorthy A. *The Journal of biological chemistry*. 2017; 292:4638–4650. [PubMed: 28154182]

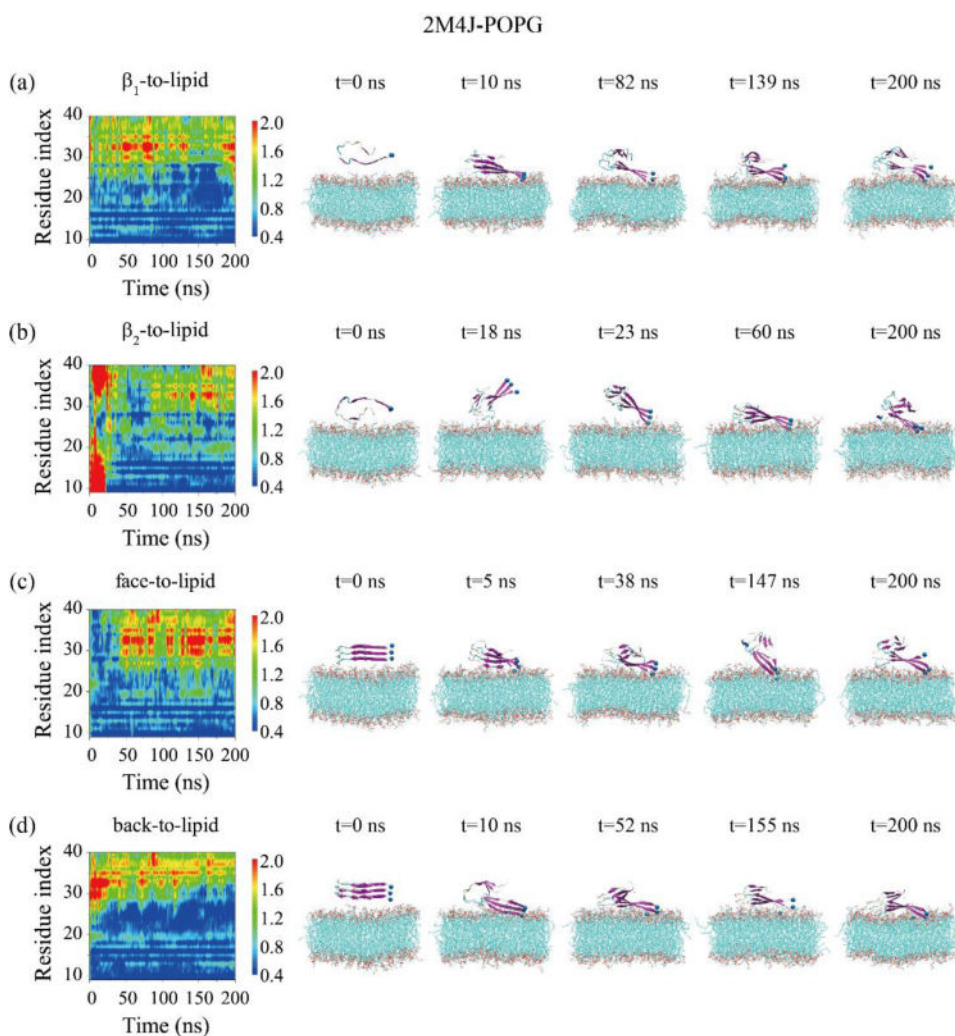


**Fig. 1.** Time evolution of the minimum distance between all atoms of each residue in the three chains and the POPG lipid bilayer for the 2BEG-POPG system starting from four initial states:  $\beta_1$ -to-lipid (a),  $\beta_2$ -to-lipid (b), face-to-lipid (c) and back-to-lipid (d). Snapshots at five time points are given to visualize the adsorption behavior of 2BEG timers on the POPG bilayer surface.

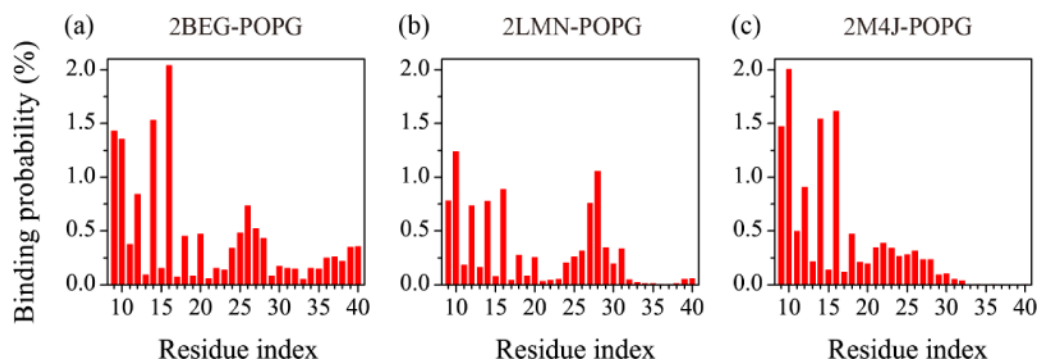


**Fig. 2.** Time evolution of the minimum distance between all atoms of each residue in the three peptide chains and the POPG lipid bilayer for the 2LMN-POPG system in MD runs starting from four states:  $\beta_1$ -to-lipid (a),  $\beta_2$ -to-lipid (b), face-to-lipid (c) and back-to-lipid (d). The snapshots at five time points are also given to visualize the adsorption process of 2LMN timers on the POPG bilayer surface.

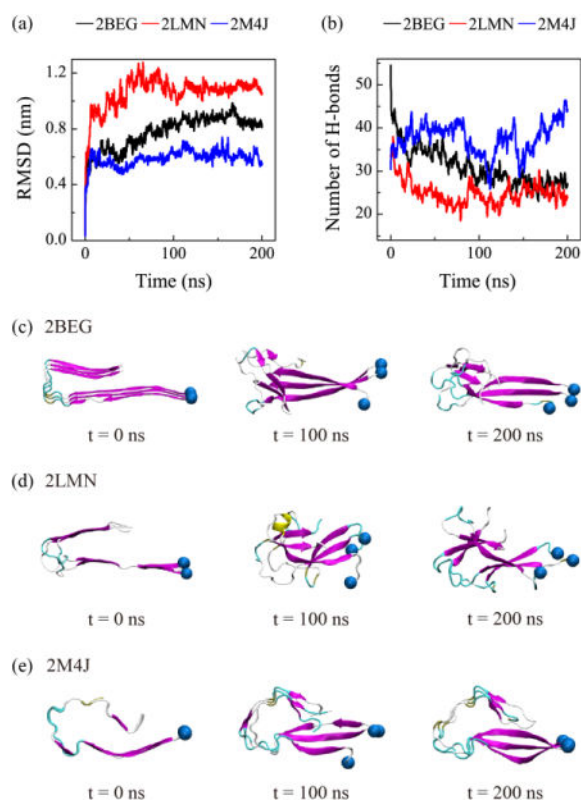




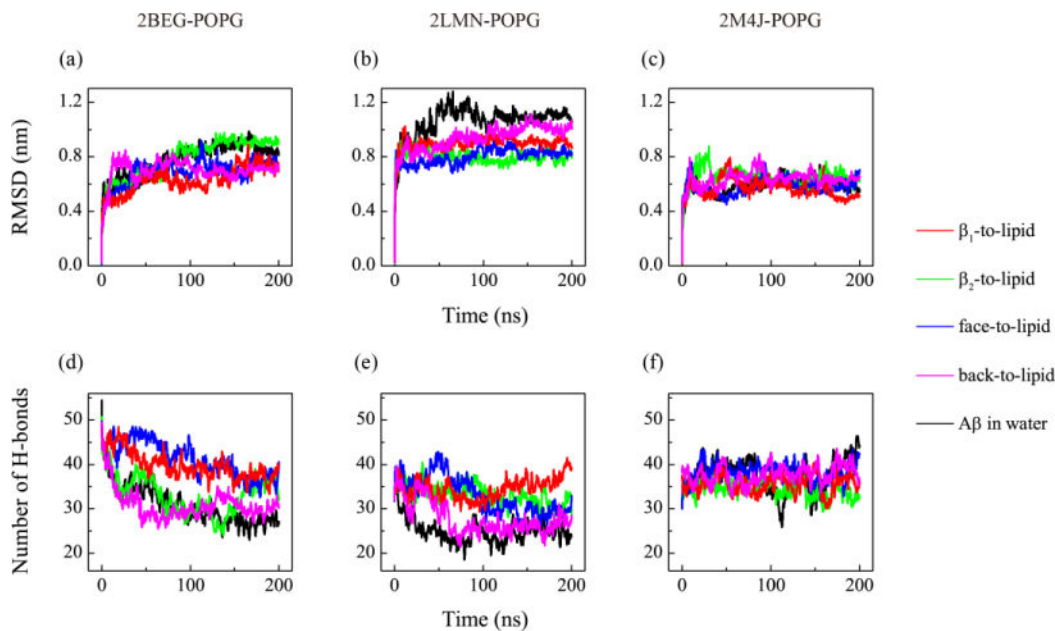
**Fig. 3.** Time evolution of the minimum distances between all atoms of each residue in the three chains and the POPG lipid bilayer for 2M4J-POPG system in MD runs starting from four different initial states:  $\beta_1$ -to-lipid (a),  $\beta_2$ -to-lipid (b), face-to-lipid (c) and back-to-lipid (d). The snapshots at five different time points are given to visualize the adsorption dynamics of 2M4J timers on the POPG bilayer surface.



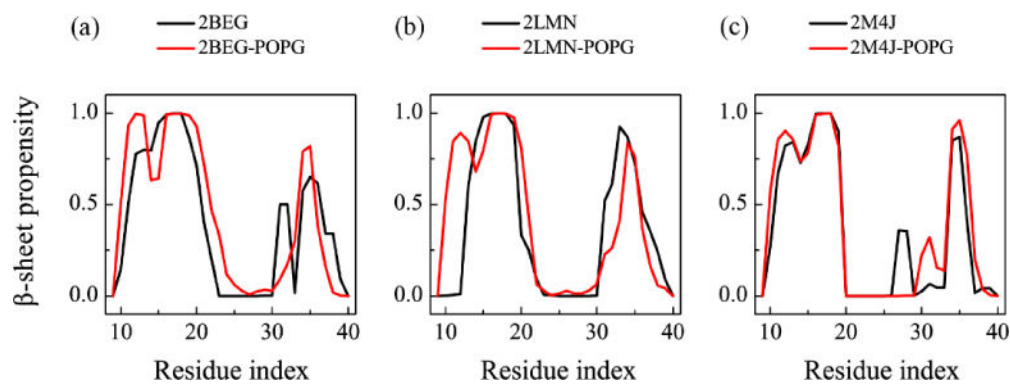
**Fig. 4.** Membrane binding probability of each amino acid residue for the three protofibrillar A $\beta$  trimers in the A $\beta$ -POPG system. The binding probabilities were calculated using all heavy atoms over the last 50 ns for each A $\beta$ -POPG system.



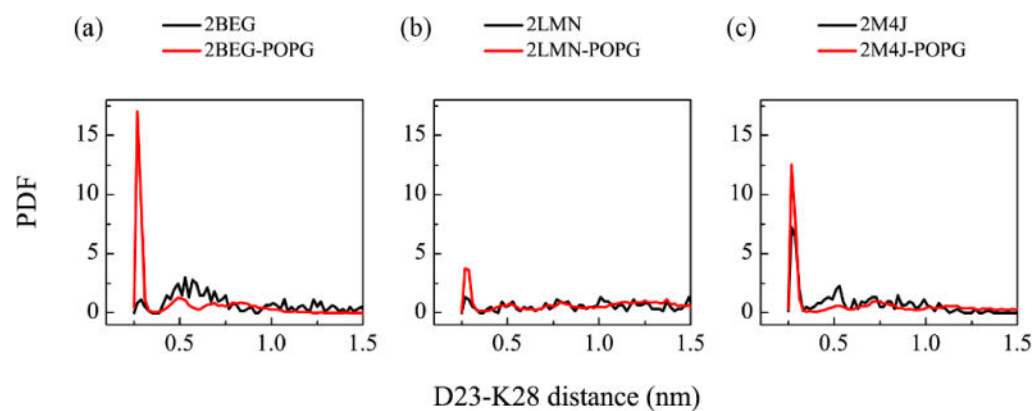
**Fig. 5.** Structural stability analysis of the three protofibrillar A $\beta_{9-40}$  trimers in water. Time evolution of the C $\alpha$ -RMSD (a) and the number of backbone hydrogen bonds (b) of each trimer. Snapshots of A $\beta$  trimers generated at 0, 100 and 200 ns for 2BEG (c), 2LMN (d) and 2M4J (e) systems are also shown. The snapshots at t=0 ns are the same as the initial states shown in Table 1 for the A $\beta$  system.



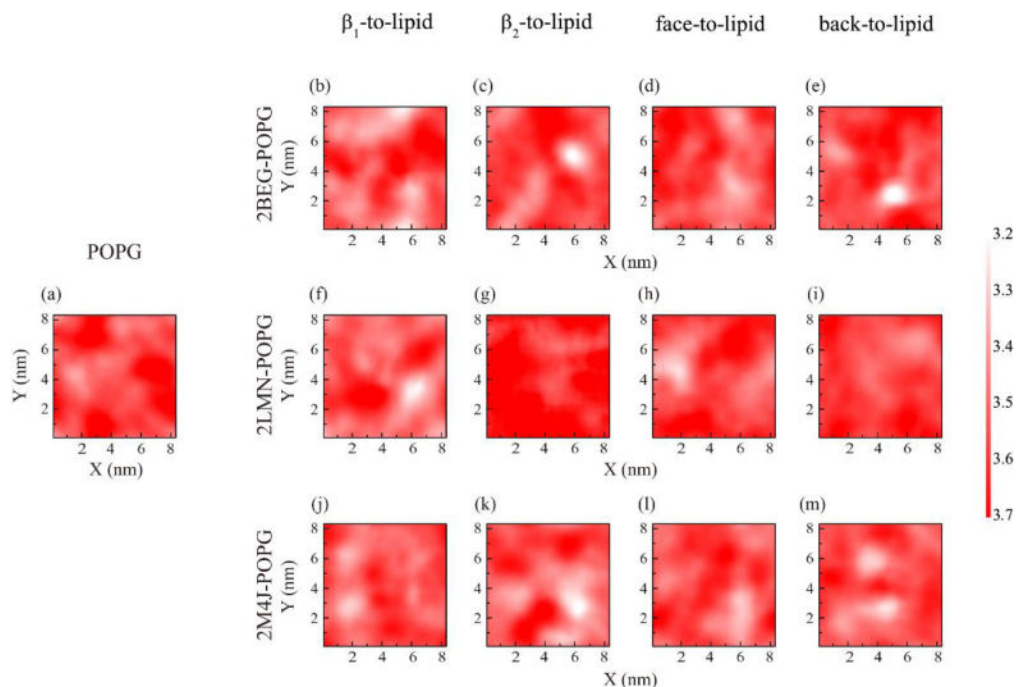
**Fig. 6.** Structural stability analysis of the three protofibrillar A $\beta_{9-40}$  trimers in the presence of POPG lipid bilayers. For each A $\beta$ -POPG system (2BEG-POPG, 2LMN-POPG, 2M4J-POPG), we show the time evolution of the C $\alpha$ -RMSD (a, b, c) and the number of backbone hydrogen bonds (d, e, f) of A $\beta$  trimer in MD runs starting from four states:  $\beta_1$ -to-lipid (red),  $\beta_2$ -to-lipid (green), face-to-lipid (blue) and back-to-lipid (pink). For comparison, the results for each A $\beta$  trimer in water without POPG bilayers are also given (black).

**Fig. 7.**

The residue-based  $\beta$ -sheet propensity of each A $\beta_{9-40}$  trimer in the absence and presence of POPG lipid bilayers. The  $\beta$ -sheet propensity of each residue was calculated using the last 50 ns simulation data for both A $\beta$  (black) and A $\beta$ -POPG systems (red). For each A $\beta$ -POPG system, the  $\beta$ -sheet propensity is the average of the four MD trajectories.

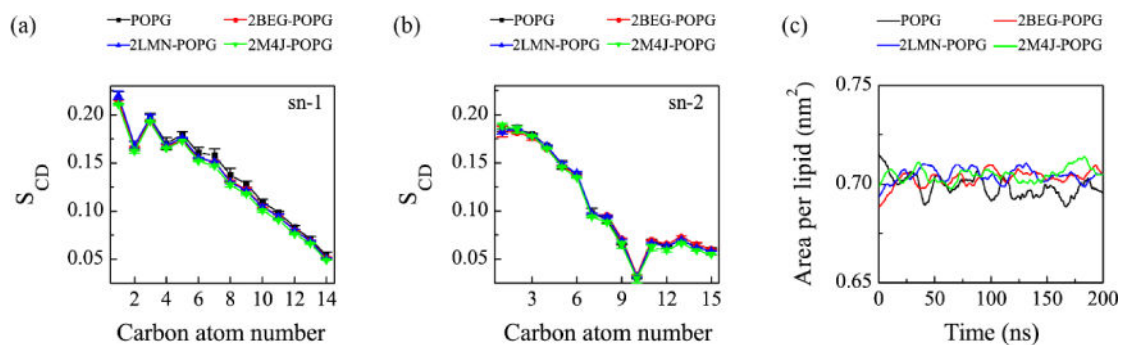


**Fig. 8.** Effect of POPG bilayers on the D23-K28 salt-bridge. Probability density function of the D23-K28 distance in A $\beta$  (black curve) and A $\beta$ -POPG (red curve) systems. The D23-K28 distance in A $\beta$ -POPG system is the average of the four MD runs. All calculations were based on the last 50 ns data of each MD run.



**Fig. 9.**

The POPG bilayer thickness distribution map over the x-y plane for each A $\beta$ -POPG system in the MD runs starting from different initial states:  $\beta_1$ -to-lipid,  $\beta_2$ -to-lipid, face-to-lipid and back-to-lipid. For comparison, the bilayer thickness distribution map of a pure POPG bilayer is also presented. The bilayer thickness was calculated using the last 50-ns data of each MD run.


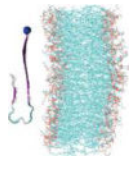
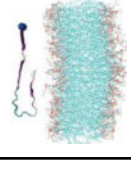
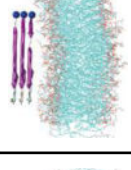
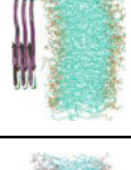

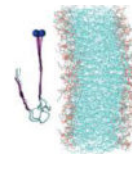
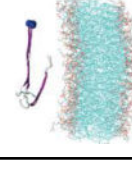
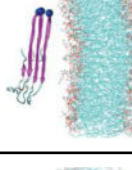
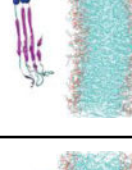

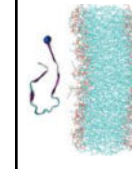
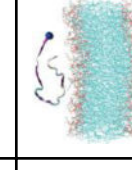
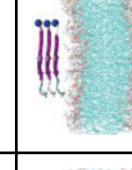
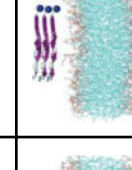
**Fig. 10.**

Influence of membrane binding of protofibrillar A $\beta$  trimers on the order of the head and the tail atoms of POPG lipids in the upper leaflet of the bilayer. The order parameter  $S_{CD}$  for the sn-1 chain (a) and sn-2 chain (b) of POPG as a function of carbon atom index. (c) Area per lipid as a function of simulation time. For each A $\beta$ -POPG system, both the  $S_{CD}$  values and the area per lipid are the average over the four different MD runs using the last 50 ns simulation data. The  $S_{CD}$  and the area per lipid of a neat POPG lipid bilayer are also given for comparison.



Table 1

Name and initial state of A $\beta$  and A $\beta$ -POPG systems. The PDB ID of each fibril model denotes the three constructed protofibrillar A $\beta$ <sub>9-40</sub> trimers. In the four initial states of each A $\beta$ -POPG system, the orientations of the protofibrillar A $\beta$  trimers with respect to the POPG bilayer surface differ. According to the initial orientations of each trimer relative to the lipid bilayer surface, the four initial A $\beta$ -POPG states are labelled as  $\beta_1$ -to-lipid,  $\beta_2$ -to-lipid, face-to-lipid and back-to-lipid. The  $\beta_1$ -to-lipid and  $\beta_2$ -to-lipid represent respectively the two systems where the N-terminal and C-terminal  $\beta$ -sheets face to the lipid bilayer surface. The face-to-lipid and back-to-lipid represent respectively the systems where the face and back of the protofibrillar A $\beta$  trimer face to the lipid bilayer surface. The A $\beta$  trimer is shown in cartoon representation, with the  $\beta$ -sheet in purple, the coil in white and the turn in cyan. The C $_{\alpha}$  atom of each G9 residue is denoted by a blue sphere. The lipids are shown in line representation, with oxygen, phosphorus, hydrogen and carbon atoms in red, tan, white and cyan, respectively. For clarity, counterions and water molecules are not shown.

A $\beta$ system		A $\beta$ -POPG system				
Name	Initial state	Name	Initial states			
			$\beta_1$ -to-lipid	$\beta_2$ -to-lipid	face-to-lipid	back-to-lipid
2BEG		2BEG-POPG				
2LMN		2LMN-POPG				
2M4J		2M4J-POPG				

**Table 2**

A summary of the MD setup details. For each system, we present the name of the system, the size of the simulation box, the total number of atoms, simulation time, the number of MD runs and the number of initial states.

System	Box size (nm <sup>3</sup> )	Total number of atoms	Simulation time (ns)	Number of MD runs	Number of initial states
2BEG	7.5×7.5×9.0	49751	200	1	1
2LMN	7.5×7.5×9.0	49769	200	1	1
2M4J	7.5×7.5×9.0	49739	200	1	1
2BEG-POPG	8.2×8.3×13.7	91001	200×4	4	4
2LMN-POPG	8.2×8.3×13.7	91001	200×4	4	4
2M4J-POPG	8.2×8.3×13.7	91001	200×4	4	4